ADVANCED FUNCTIONAL MATERIALS
www.afm-journal.de

Crystallization-Induced Phase Separation in Solution-Processed Small Molecule Bulk Heterojunction Organic Solar Cells

*Alexander Sharenko, Martijn Kuik, Michael F. Toney, and Thuc-Quyen Nguyen**

The driving forces and processes associated with the development of phase separation upon thermal annealing are investigated in solution-processed small molecule bulk heterojunction (BHJ) organic solar cells utilizing a diketopyrrolopyrrole-based donor molecule and a fullerene acceptor (PCBM). In-situ thermal annealing X-ray scattering is used to monitor the development of thin film crystallization and phase separation and reveals that the development of blend phase separation strongly correlates with the nucleation of donor crystallites. Additionally, these morphological changes lead to dramatic increases in blend electron mobility and solar cell figures of merit. These results indicate that donor crystallization is the driving force for blend phase separation. It is hypothesized that donor crystallization from an as-cast homogeneous donor:acceptor blend simultaneously produces donor-rich domains, consisting largely of donor crystallites, and acceptor-rich domains, formed from previously mixed regions of the film that have been enriched with acceptor during donor crystallization. Control of donor crystallization in solution-processed small molecule BHJ solar cells employing PCBM is thus emphasized as an important strategy for the engineering of the nanoscale phase separated, bicontinuous morphology necessary for the fabrication of efficient BHJ photovoltaic devices.

1. Introduction

Bulk heterojunction organic photovoltaics (BHJ OPVs) have been the subject of much academic and industrial interest because of their potential to serve as a flexible, low cost, scalable source of electrical power.[1,2] These devices consist of a nanoscale phase separated, bicontinuous network of electron donating and electron accepting molecules. This nanoscale morphology is necessitated by the operational mechanisms of a BHJ OPV device.[3] Photoexcitation of either the donor or acceptor molecule produces a bound electron-hole pair known as an exciton. Excitons can be split into free charge carriers at the type II heterojunction formed between donor and acceptor molecules provided the exciton can diffuse to this interface before decaying back to the ground state. Once the exciton has split into a hole and an electron, these free charge carriers traverse through the donor and acceptor phase, respectively, and are collected at the electrodes. The BHJ morphology must therefore consist of domains small enough to allow efficient exciton harvesting and charge generation, but large enough to form bicontinuous donor and acceptor networks for the efficient extraction of free charge carriers. Accordingly, BHJ performance usually correlates with the presence of donor and acceptor domain sizes that do not significantly exceed the exciton diffusion length, approximately 10–20 nm.[4,5]

Given the strong dependence of BHJ OPV performance on blend phase separation, it is imperative to understand the thermodynamic driving forces and processes that lead to the formation of nanoscale phase separated, bicontinuous morphologies. Investigations of the much studied poly(3-hexylthiopene):phenyl-C_{61}-butyric acid methyl ester (P3HT:PC_{61}BM) blend have found that in this system phase separation is largely the result of crystallization of the semicrystalline donor P3HT.[6–8] Solid state miscibility between the donor and acceptor has, however, also been demonstrated to directly affect BHJ morphology including the degree of donor–acceptor phase separation as well as the relative purity of mixed regions of amorphous donor and acceptor.[4,9–12] As polymer:fullerene BHJ blends dominate the literature,[13] much less is known about the development of phase separation in OPVs that utilize solution-processed small molecule donor materials. Small molecule donors have, however, recently emerged as a viable alternative[14,15] to their polymer counterparts and offer several potential advantages in that they are monodisperse and can be purified with standard organic chemistry techniques. Knowledge of the driving forces for phase

A. Sharenko
Materials Department
University of California
Santa Barbara, CA 93106, USA
A. Sharenko, Dr. M. Kuik, Prof. T.-Q. Nguyen
Center for Polymers and Organic Solids
University of California
Santa Barbara, CA 93106, USA
E-mail: quyen@chem.ucsb.edu
Dr. M. F. Toney
Stanford Synchrotron Radiation Lightsource
SLAC National Accelerator Laboratory
Menlo Park, CA 94025, USA

DOI: 10.1002/adfm.201304100

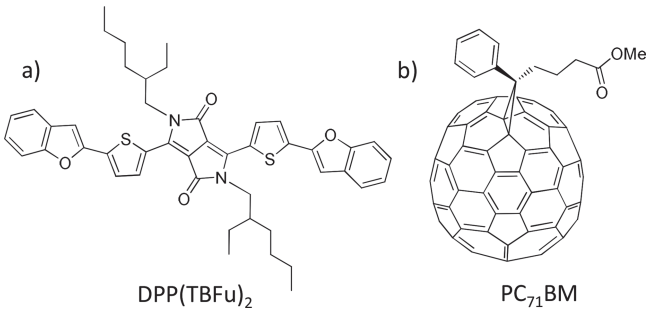

Figure 1. Chemical structures of the electron donor, a) DPP(TBFu)$_2$, and electron acceptor, b) PC$_{71}$BM, used in this study.

separation in solution-processed small molecule BHJ OPVs will therefore aid in the engineering of future high performing solar cells.

In this study we investigate phase separation in a solution-processed BHJ blend consisting of the small molecule donor DPP-OT-3,6-bis(5-(benzofuran-2-yl)thiophen-2-yl)-2,5-bis(2-ethylhexyl)pyrrolo[3,4-c]pyrrole-1,4-dione (DPP(TBFu)$_2$) and the fullerene electron acceptor PC$_{71}$BM (**Figure 1**). This system was chosen because previous studies suggested that in optimized devices thermal annealing leads to increased phase separation and dramatic gains in power conversion efficiency (PCE).[16,17] However, until now we have not investigated the driving forces for this behavior and could therefore not fully explain the specific processes responsible for this change in blend morphology and device performance. In the work presented herein, we use in-situ thermal annealing grazing incidence X-ray scattering to investigate the development of blend crystallinity and phase separation as a function of temperature and donor:acceptor blend ratio in order to better understand how thermal annealing leads to the formation of a BHJ morphology. Using these data we are able to correlate the formation of DPP(TBFu)$_2$ crystallites with the onset of phase separation in DPP(TBFu)$_2$:PC$_{71}$BM blends. Based on these X-ray scattering data as well as charge carrier mobility data extracted from current density-voltage (*J*–*V*) curves of single carrier diodes undergoing in-situ thermal annealing, we hypothesize that, on the time scales and temperature ranges associated with the fabrication of optimized BHJ OPVs, blend phase separation is largely the result of donor crystallization. This observation is then used to explain the dramatic increase in performance induced by thermal annealing in higher performing donor:acceptor ratio DPP(TBFu)$_2$:PC$_{71}$BM BHJ OPVs as we directly correlate changes in blend morphology with solar cell figures of merit.

2. Results and Discussion

In order to characterize the bulk morphology of DPP(TBFu)$_2$:PC$_{71}$BM BHJ OPVs, various blend ratio films were probed with two complementary grazing incidence X-ray scattering techniques.[18] Grazing incidence wide angle X-ray scattering (GIWAXS) is an X-ray diffraction technique and therefore provides information about thin film crystallinity.[19] Grazing incidence small angle X-ray scattering (GISAXS) is sensitive to electron density inhomogeneities on length scales on the order of 10 nm to 1 µm making it an appropriate technique to investigate donor–acceptor phase separation in BHJ OPVs.[20] A grazing incidence geometry allows the selection of incidence angles greater than the critical angle of the BHJ blend but less than the critical angle of the substrate, thus ensuring scattered intensity is dominated by morphological features within the bulk of the BHJ film. Additionally, the grazing incidence geometry is particularly amenable to in-situ studies as it does not require thin films to be removed from their substrate and minimizes exposure times because of the increased scattered intensity from the standing wave formed within the film. In order to monitor blend morphological evolution as a function of temperature and therefore provide insight into the processes associated with the development of phase separation in solution-processed small molecule BHJ OPVs, both GIWAXS and GISAXS were performed on samples undergoing in-situ thermal annealing. This allowed donor or acceptor crystallization and donor–acceptor phase separation to be monitored during morphological development.

DPP(TBFu)$_2$ crystallinity was quantified by fitting the DPP(TBFu)$_2$ (100) peak from GIWAXS spectra taken at various temperatures with a Pseudo-Voigt function (Figure S1, Supporting Information). The Pseudo-Voigt peak area is a relative measure of the crystalline volume within the thin film. In neat films as well as in blends with PC$_{71}$BM, DPP(TBFu)$_2$ exhibits no signs of crystallinity in the as-cast state when spin-cast from chloroform. However, upon thermal annealing DPP(TBFu)$_2$ undergoes a cold crystallization similar to what has previously been observed in PC$_{61}$BM (**Figure 2**a).[21] We define the cold crystallization temperature (T_{CC}) as the temperature at which the DPP(TBFu)$_2$ (100) peak appears above the background scattering. In neat DPP(TBFu)$_2$ films the T_{CC} occurs at 50 °C. In DPP(TBFu)$_2$:PC$_{71}$BM blend films the DPP(TBFu)$_2$ T_{CC} increases with increasing PC$_{71}$BM content to 70 °C, 75 °C, and 100 °C in 70:30, 50:50, and 30:70 DPP(TBFu)$_2$:PC$_{71}$BM blends by weight respectively (Figure 2b–d). The trend of increasing DPP(TBFu)$_2$ T_{CC} with increasing PC$_{71}$BM content can be explained in terms of DPP(TBFu)$_2$ dilution. As PC$_{71}$BM content increases, the concentration of DPP(TBFu)$_2$ nuclei likely decreases and thus the overall DPP(TBFu)$_2$ crystallization rate decreases, therefore increasing DPP(TBFu)$_2$'s T_{CC}. Similar T_{CC} trends have previously been observed in partially miscible polymer blends and explained as such.[22,23] The crystalline correlation length (CCL) of DPP(TBFu)$_2$ was also calculated from Scherrer's equation:

$$\mathrm{CCL} = \frac{2\pi}{\mathrm{FWHM}} \quad (1)$$

Where FWHM is the full-width-at-half-maximum of the fitted Pseudo-Voigt function. The CCL is a measure of crystallite size and/or perfection.[24] The CCL of DPP(TBFu)$_2$ in both neat and blend films follows a very similar trend to the relative peak area. This indicates that most of the increase in peak area after the T_{CC} can be attributed to the growth of existing DPP(TBFu)$_2$ crystallites as opposed to the nucleation of new crystallites. In the neat DPP(TBFu)$_2$ film and 70:30 blend samples the (100) peak area and CCL increase dramatically beginning at the T_{CC} and continuing over a narrow temperature

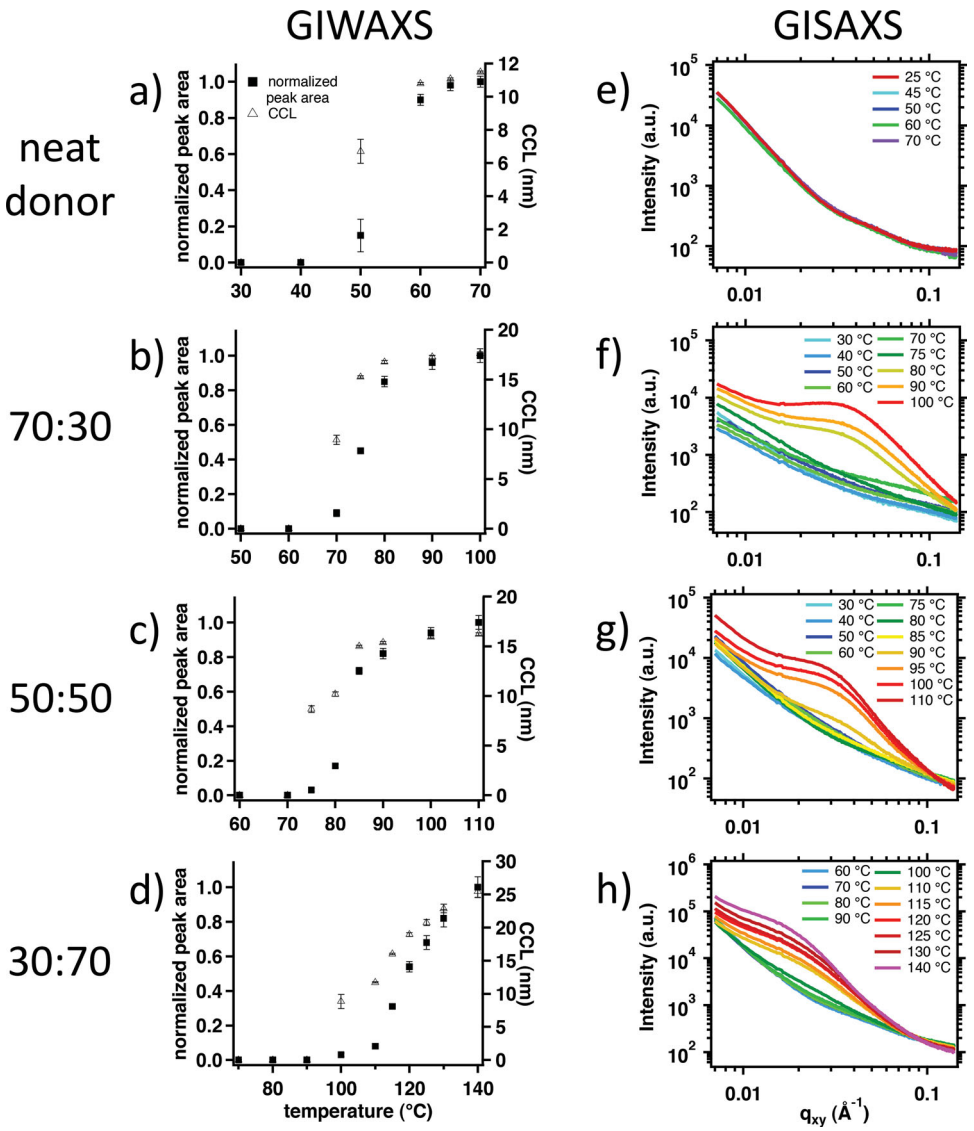

Figure 2. In-situ thermal annealing a–d) GIWAXS and e–h) GISAXS of a a,e) neat DPP(TBFu)$_2$ film as well as b–d,f–h) DPP(TBFu)$_2$:PC$_{71}$BM blend films.

range of approximately 10 degrees. They then only slightly increase as the temperature is further increased. The 50:50 blend sample's peak area and CCL exhibit the same dramatic increases beginning at the T_{CC} but then continue to gradually increase as temperature is further increased. The 30:70 blend exhibits somewhat different behavior from the other samples in that its peak area and CCL continually increase with an increase in temperature above T_{CC} without exhibiting the dramatic increases followed by a small or gradual increase characteristic of the other samples. Therefore as the fraction of PC$_{71}$BM in the film increases, the nucleation of DPP(TBFu)$_2$ crystallites requires higher temperatures and becomes a more gradual process. Importantly, no PC$_{71}$BM crystallization was observed in any of the DPP(TBFu)$_2$:PC$_{71}$BM blend films in the temperature ranges investigated during this study (Figure S2, Supporting Information).

To facilitate a direct comparison of thin film crystallinity and phase separation, in-situ thermal annealing GISAXS measurements were performed on samples fabricated identically to those used for in-situ GIWAXS and measured over the same temperature range (Figure 2e–h). Extracting quantitative information from GISAXS profiles requires fitting experimental data to a model, however, modeling a BHJ OPV blend is extremely challenging given the irregularly shaped, polydisperse, interconnected and randomly distributed domains characteristic of a BHJ morphology. Due to these complexities there exists no widely accepted GISAXS model for BHJ OPV blends, and we therefore elect to interpret our data qualitatively. GISAXS scattering contrast is produced via electron density differences, therefore, to a first order approximation, blend films will produce a peak or shoulder in scattered intensity at a q value corresponding to the average length scale associated with the differences in electron density, that is, the length scale of phase separation. Additionally, the intensity of this peak or shoulder within a given sample undergoing a series of in-situ measurements is proportional to the extent of blend phase separation.

Figure 2e shows in-situ thermal annealing GISAXS data for a neat film of DPP(TBFu)$_2$ from 25 to 70 °C. The in-plane line scans show no significant change even though in-situ thermal annealing GIWAXS measurements have shown that DPP(TBFu)$_2$ undergoes a cold crystallization in this temperature range. We therefore conclude that the electron density differences between amorphous and crystalline regions of DPP(TBFu)$_2$ are not significant enough to produce a peak in scattered intensity. We can then reason that any peaks in the scattered intensity exhibited by DPP(TBFu)$_2$:PC$_{71}$BM blend films are the result of electron density differences between DPP(TBFu)$_2$-rich and PC$_{71}$BM-rich phases. Figures 2f–h display in-situ thermal annealing GISAXS data of 70:30, 50:50, and 30:70 DPP(TBFu)$_2$:PC$_{71}$BM blend films. Each blend ratio exhibits similar behavior. As-cast blends display only the same monotonically decreasing intensity seen in films of neat DPP(TBFu)$_2$. Thus, the as-cast blends lack sufficient electron density to produce a peak in scattered intensity indicating that these samples consist of an intimately mixed donor–acceptor morphology. As the blends are heated, however, a peak develops at some transition temperature indicating the appearance of differences in electron density in the film which we interpret as the onset of donor–acceptor phase separation. The GISAXS peak shifts slightly to smaller q values with increasing PC$_{71}$BM content indicating phase separation is occurring on a larger length scale with increasing PC$_{71}$BM content. Most interestingly, in each blend the temperature at which this transition from homogeneously mixed to phase separated morphology occurs closely correlates with the nucleation of DPP(TBFu)$_2$ crystallites as measured using the in-situ thermal annealing GIWAXS discussed above. The development of phase separation in each of the different blend ratios also follows the same trend exhibited by the in-situ GIWAXS measurements. Specifically, the 70:30 blend transitions from a homogeneous blend to a phase separated morphology over a relatively narrow temperature range and the 50:50 blend transitions slightly more gradually whereas the 30:70 blend gradually and continuously phase separates with increasing temperature. In both the 70:30 and 50:50 blends, phase separation occurs at the temperature immediately following the dramatic increase in peak area exhibited by in-situ GIWAXS. The 30:70 blend, however, begins to phase separate at the temperature that corresponds to the onset of DPP(TBFu)$_2$ crystallization, that is, DPP(TBFu)$_2$'s T_{CC}.

Photoluminescence (PL) measurements of as-cast blend films as well as blend films that had been annealed above their respective DPP(TBFu)$_2$$T_{CC}$ were used to further verify our interpretation of the presented GISAXS data (**Figure 3**). For each blend, annealed films exhibit PL spectra identical to that of neat DPP(TBFu)$_2$. The PL spectra of as-cast blends, however, are shifted to lower energy and broadened compared to those of the annealed blends and neat DPP(TBFu)$_2$. We assign this lower energy, broader PL spectra as originating from the DPP(TBFu)$_2$:PC$_{71}$BM charge transfer (CT) state.[25,26] In order for the CT state emission to dominate emission from DPP(TBFu)$_2$, the blend must consist of a well-mixed morphology that maximizes DPP(TBFu)$_2$:PC$_{71}$BM interfacial surface area while lacking neat DPP(TBFu)$_2$ domains larger than the exciton diffusion length.[27,28] Conversely, for neat DPP(TBFu)$_2$ emission to dominate CT state emission, the blend morphology

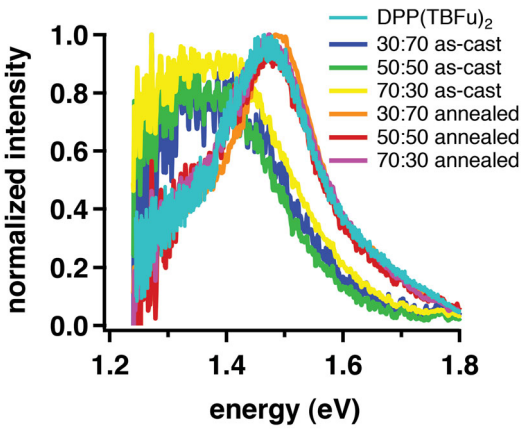

Figure 3. Photoluminescence spectra of a neat DPP(TBFu)$_2$ film as well as as-cast and annealed DPP(TBFu)$_2$:PC$_{71}$BM blend films. The annealed 70:30, 50:50, and 30:70 blend films were annealed at 100, 110, and 150 °C respectively for 2 min each in a nitrogen environment.

must consist of a significant amount of DPP(TBFu)$_2$ domains larger than the exciton diffusion length. PL and GISAXS measurements then both indicate that as-cast blends consist of an intimately mixed morphology, but that when blend films are annealed above DPP(TBFu)$_2$'s T_{CC} they phase separate. These measurements of bulk morphological properties are also consistent with previous atomic force microscopy measurements of surface topography which indicated phase separation upon thermal annealing.[16] However, we have now importantly correlated the development of bulk phase separation with the onset of DPP(TBFu)$_2$ crystallization. We thus hypothesize that the development of DPP(TBFu)$_2$:PC$_{71}$BM blend phase separation is the direct result of DPP(TBFu)$_2$ crystallization from an initially homogeneously mixed, amorphous donor:acceptor film. We propose that as DPP(TBFu)$_2$ nuclei form and grow they expel PC$_{71}$BM molecules, simultaneously creating DPP(TBFu)$_2$-rich domains, consisting largely of DPP(TBFu)$_2$ crystallites, and PC$_{71}$BM-rich domains, formed from previously mixed regions of the film that have been enriched with PC$_{71}$BM during DPP(TBFu)$_2$ crystallization.

If phase separation is the result of DPP(TBFu)$_2$ crystallization, the nucleation and growth of DPP(TBFu)$_2$ crystallites should correlate with an increase in blend electron mobility as increased phase separation leads to aggregation and percolation of PC$_{71}$BM, the electron transporting phase. To confirm this behavior, electron-only diodes of a 70:30 DPP(TBFu)$_2$:PC$_{71}$BM blend were fabricated. Diode J–V curves were then measured during in-situ thermal annealing over the same temperature range investigated with in-situ thermal annealing GIWAXS and GISAXS and mobility values extracted by fitting these data to the Mott-Gurney relation for space charge-limited current (**Figure 4**). In the as-cast 70:30 blend film the electron mobility is 2.0×10^{-6} cm^2 V^{-1} s^{-1}, 3 orders of magnitude lower than the diode electron mobility of a neat PCBM film, likely due to a lack of percolated PC$_{71}$BM networks in the homogeneous as-cast morphology.[29] The electron mobility remains low with increasing thermal annealing temperature until dramatically increasing approximately 2 orders of magnitude at 90 °C to 3.3×10^{-4} cm^2 V^{-1} s^{-1}. In organic semiconductors, charge carriers

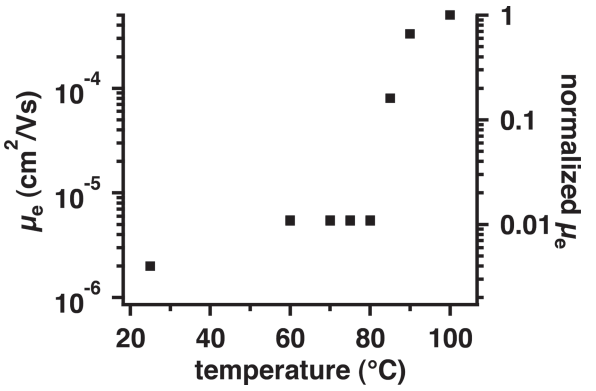

Figure 4. Electron mobility (μ_e) of a 70:30 DPP(TBFu)$_2$:PC$_{71}$BM diode measured during in-situ thermal annealing.

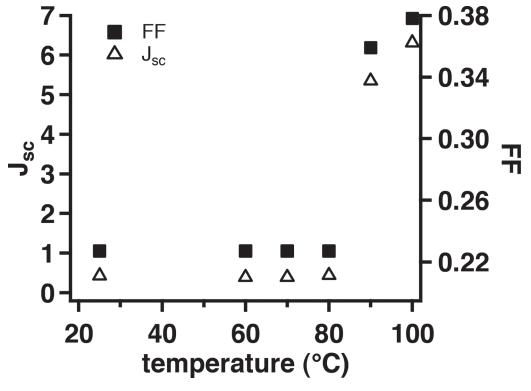

Figure 5. J_{sc} and FF of a 70:30 DPP(TBFu)$_2$:PC$_{71}$BM BHJ OPV device series annealed at the indicated temperatures.

move by a thermally activated hopping process between localized states. Thus, some increase in mobility is expected with increasing sample temperature. Based on PCBM's hopping activation energy we would expect the electron mobility to approximately double with an increase in temperature from 80 to 100 °C.[30] The observed increase in electron mobility is thus far greater than can be explained by increased thermal hopping activation alone. Based on this observation as well as the fact that the mobility increases from a value orders of magnitude lower than that of neat PCBM to approaching that of neat PCBM, we explain this dramatic increase in electron mobility as a consequence of the development of percolated networks of PC$_{71}$BM that form as a result of DPP(TBFu)$_2$ crystallization and concurrent PC$_{71}$BM aggregation. This interpretation of the data is further supported given the close correlation of the dramatic increase in the relative crystallinity of DPP(TBFu)$_2$ as measured by in-situ thermal annealing GIWAXS, the temperature at which phase separation develops as determined by in-situ thermal annealing GISAXS and the temperature at which the electron mobility significantly increased. The slightly higher temperature at which the increase in electron mobility is observed as compared to the development of phase separation measured with GISAXS could be because further phase separation needs to occur before the aggregated PC$_{71}$BM domains form a percolated network necessary for high electron mobility in the blend. We have therefore demonstrated that not only does DPP(TBFu)$_2$ crystallization lead to blend phase separation but that in 70:30 blends this phase separation then leads to a dramatic increase in electron mobility, presumably due to the formation of a percolated network of aggregated PC$_{71}$BM domains.

Previous work demonstrated that BHJ OPV performance in the as-cast 70:30 blend is very low but that upon thermal annealing both short-circuit current density (J_{sc}) and fill factor (FF) (and therefore PCE) dramatically increase.[16] We therefore serially annealed a 70:30 DPP(TBFu)$_2$:PC$_{71}$BM BHJ OPV device over a temperature range similar to what we have already investigated with in-situ thermal annealing GIWAXS, GISAXS and electron only diode measurements so that we can compare the increase in solar cell figures of merit with the changes in film morphology and charge transport discussed above (Figure S3, Supporting Information). **Figure 5** displays the J_{sc} and FF of a 70:30 OPV device that was serially annealed at the given temperature values. The J_{sc} and FF are initially very low, 0.43 mA cm^{-2} and 0.23, respectively, but dramatically increase to 5.35 mA cm^{-2} and 0.36 when annealed at 90 °C. This is the same temperature the blend electron mobility was observed to dramatically increase via in-situ thermal annealing of electron only diodes of 70:30 DPP(TBFu)$_2$:PC$_{71}$BM blends. The strong correlation between the dramatic increases in electron mobility and J_{sc} and FF is consistent with previous investigations that have shown that, in general, recombination decreases, and thus J_{sc} and FF increase, as charge carrier mobility increases.[31,32] While we are now comparing an ex-situ measurement (serial annealing) to an in-situ measurement (blend electron mobility), the strong correlation between data from the two types of measurements suggests this is a valid comparison. Some of this increase in J_{sc} and FF, however, is probably additionally attributed to the approximately order of magnitude increase in hole mobility that also occurs over this temperature range, likely due to the increase in the solid state order of DPP(TBFu)$_2$, the hole transporting phase (Table S1, Supporting Information). The lower OPV performance exhibited here compared to previous reports[16] can be attributed to the shorter, serialized annealing in this study as opposed to the optimized, longer, single annealing step previously used to achieve higher efficiency. We have now shown that donor crystallization, the development of blend phase separation and a significant increase in blend electron mobility and OPV figures of merit all dramatically increase over the same narrow temperature range during thermal annealing.

In order to investigate the influence DPP(TBFu)$_2$:PC$_{71}$BM solid state immiscibility has on phase separation 70:30, 50:50, and 30:70 blend films were annealed for 48 hours at 60 °C. If solid state immiscibility between the two materials is acting as a significant driving force for phase separation, perhaps via a spinodal decomposition process, it was hypothesized that samples held at an elevated temperature that facilitated solid state diffusion, but below DPP(TBFu)$_2$'s T_{CC}, and allowed time to approach equilibrium, would exhibit blend phase separation without DPP(TBFu)$_2$ crystallization. This experiment was therefore an attempt to decouple DPP(TBFu)$_2$ crystallization and blend phase separation. **Figure 6** shows the GISAXS line scans and GIWAXS 1D integrations of these samples. By comparing as-cast and annealed line cuts in Figure 6a we

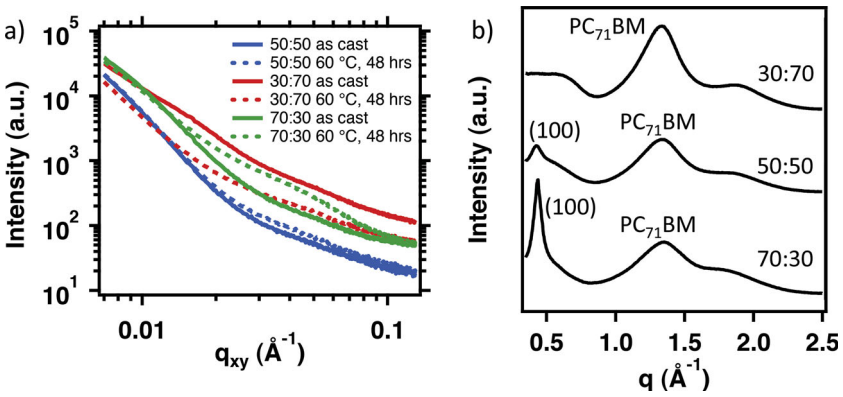

Figure 6. a) GISAXS in-plane line scans of as-cast DPP(TBFu)$_2$:PC$_{71}$BM blend films as well as blend films annealed at 60 °C for 48 h. b) 1D GIWAXS radial integrations of DPP(TBFu)$_2$:PC$_{71}$BM blend films annealed at 60 °C for 48 h.

can deduce that the 70:30 blend ratio sample developed some amount of phase separation based on the small peak it displays that is not present in the as-cast sample. Likewise, the 50:50 blend exhibits an even smaller degree of phase separation based on the slight increase in intensity of the annealed film at high q values compared to the as-cast film. However, the 30:70 blend display a negligible amount of phase separation during the 48 h, 60 °C anneal based on the very similar shape of the as-cast and annealed line cuts. Interestingly, Figure 6b shows that the 70:30 film displays some amount of DPP(TBFu)$_2$ crystallization based on the strength of the DPP(TBFu)$_2$ (100) peak and the 50:50 blend exhibits a small amount of DPP(TBFu)$_2$ crystallization based on the very weak (100) peak intensity. The 30:70 blend, however, displays no signs of DPP(TBFu)$_2$ crystallization as the peaks at 0.68, 1.31 and 1.90 Å^{-1} associated with PC$_{71}$BM dominate the spectra and the DPP(TBFu)$_2$ (100) peak is absent. As phase separation once again correlates with DPP(TBFu)$_2$ crystallization and is absent in blends that lack DPP(TBFu)$_2$ crystallization, we hypothesize that while DPP(TBFu)$_2$ and PC$_{71}$BM may be less than perfectly miscible, DPP(TBFu)$_2$ crystallization is the primary driving force for the development of blend phase separation. This is not to say that miscibility plays no role in the development of blend phase separation, however, as the degree to which PC$_{71}$BM is soluble in the amorphous DPP(TBFu)$_2$:PC$_{71}$BM matrix will affect how easily PC$_{71}$BM-rich domains form,[33,34] and thus how easily PC$_{71}$BM percolation is achieved as PC$_{71}$BM is aggregated during DPP(TBFu)$_2$ crystallization. Nonetheless, as the data indicate that the development of a nanoscale phase separated, bicontinuous morphology is initiated by the formation of DPP(TBFu)$_2$ crystallites, we assign DPP(TBFu)$_2$ crystallization as the primary driving force and thus the essential process responsible for the development of blend phase separation in the samples studied here. We also note that these results imply that DPP(TBFu)$_2$'s T_{CC} has some kinetic dependence, that is, the T_{CC} can be shifted to lower temperatures given sufficiently long annealing times, which follows from well-established crystallization theory.[35] As all in-situ thermal annealing experiments were performed on extremely similar time scales, this kinetic dependence does not affect our interpretation of the presented data.

3. Conclusion

Using in-situ thermal annealing GIWAXS, GISAXS and electron only diode measurements as well as PL spectra of as-cast and annealed films we have shown that in DPP(TBFu)$_2$:PC$_{71}$BM blends donor crystallization is the driving force for the development of the nanoscale phase separated, bicontinuous morphology necessary for the fabrication of efficient BHJ OPVs. We have specifically shown that thermal annealing causes donor crystallization in neat donor films as well as donor:acceptor blend films and that in blend films this crystallization leads to the formation of donor-rich and acceptor-rich domains. In higher performing donor:acceptor ratio devices the formation of these acceptor-rich domains leads to dramatic increases in blend electron mobility and device J_{sc} and FF (and thus overall device performance). Our results therefore suggest that small molecule donor crystallization is important for reasons other than the increase in charge carrier mobility associated with order in molecular species. We have shown that phase separation in the DPP(TBFu)$_2$:PC$_{71}$BM system is induced via donor crystallization much like what has been observed in the P3HT:PCBM BHJ OPV system. However, P3HT is semicrystalline and therefore generally not considered representative of the largely structurally disordered donor polymers utilized by high performing polymer:PCBM BHJ OPVs.[4,12,33,36] In contrast, we propose that because many small molecule donors have shown evidence of crystallization, the trends we have observed in the DPP(TBFu)$_2$:PC$_{71}$BM system are likely more generally applicable to other small molecule donor:PCBM systems. This is additionally evidenced by the correlation between crystallization and phase separation exhibited by other efficient small molecule donor:PCBM BHJ OPVs.[37] Our results then further illustrate that control over donor crystallization, whether via molecular design,[38] the use of solvent additives[39] or thermal annealing,[40] is a useful strategy when attempting to control the development of an efficient small molecule:PCBM BHJ morphology.

4. Experimental Section

PC$_{71}$BM was purchased from Solenne BV and used as received. DPP(TBFu)$_2$ was synthesized as previously reported and all characterization was performed on spin-cast films from solutions identical to those previously reported for use in solar cell fabrication.[16] All films consisted of BHJ layers approximately 100 nm thick as measured with an Ambios XP-100 stylus profilometer. For all GIWAXS and GISAXS measurements samples were spin-cast onto silicon substrates previously coated with PEDOT:PSS to mimic a solar cell architecture. Silicon substrates were used to reduce background scattering from the substrate. For in-situ thermal annealing GIWAXS, GISAXS and electron only diode measurements we estimate our absolute temperature values have an error of ±3 °C. This is largely the result of temperature fluctuations as a function of position on the film as well as over time. For all in-situ thermal annealing measurements samples were heated to a desired temperature, allowed to equilibrate for 2 min and then data

collected. GIWAXS and GISAXS exposure times varied from 15 to 120 seconds based on the scattering strength of the samples. All GIWAXS and GISAXS images were normalized for exposure time during data processing.

In-Situ Thermal Annealing GIWAXS: All GIWAXS measurements were performed at Stanford Synchrotron Radiation Lightsource beamline 11–3 using a photon energy of 12.7 keV with a sample to detector distance of approximately 400 mm. A custom built heating stage was utilized as described elsewhere.[21] Experiments were performed under a helium environment to minimize background scattering and sample damage from the X-ray beam. An incident angle of 0.12° (above the critical angle of the BHJ blend, but below the critical angle of the substrate to ensure probing of the BHJ blend and not the substrate) was used in all cases. Images were collected with a MAR-345 2D image plate and processed with the software package WxDiff, provided by Dr. Stefan Mannsfeld.

In-Situ Thermal Annealing GISAXS: GISAXS measurements were performed at the Advanced Photon Source on beam line 8-ID-E using a photon energy of 7.35 keV with a sample to detector distance of approximately 2180 mm. Experiments took place in a heated chamber evacuated to approximately 3×10^{-2} Torr in order to minimize background scattering and sample damage from the X-ray beam. Thermal paste was applied between substrate and sample heating stage in order to ensure good thermal contact. An incident angle of 0.20° (above the critical angle of the BHJ blend, but below the critical angle of the substrate to ensure probing of the BHJ blend and not the substrate) was used in all cases. Images were recorded on a 2D Pilatus 1M detector and processed with the Nika software package for WaveMetrics Igor Pro.[41]

Photoluminescence: PL measurements were performed on thin films spin-cast onto cleaned glass substrates. Sample annealing was done on a calibrated hot plate for 2 min in a nitrogen environment. PL spectra were collected using a home-built fluorescence spectrometer. The emission was excited by a 633 nm He-Ne laser (JD Uniphase) output attenuated by a neutral density filter and cleaned from the plasma emission by a band-pass interference filter (Thorlabs Inc.). The PL was collected at a right angle and focused at the entrance slit of a monochromator by a 2 lens system. A long wavelength-pass interference filter (Omega Filters) was used to block the laser light reflected from the sample. The light dispersed by the monochromator (Acton Research SP-500) was detected by a charge-couple device camera (Princeton Instruments PIXIS:400). The spectra were corrected for the instrument response function by collecting reference spectra from a calibrated black body-like light source (Ocean Optics HL-2000) and calculating correction factors. Data was then converted from nm to eV.

Photovoltaic Device Fabrication and Testing: BHJ OPV devices were fabricated on UV-O_3 treated ITO substrates coated with approximately 45 nm of PEDOT:PSS (Clevios P VP Al 4083). DPP(TBFu)$_2$:PC$_{71}$BM solutions were spin cast on to PEDOT:PSS coated ITO substrates and then 100 nm of Al was thermally evaporated on top of the organic layer at a pressure of approximately 1×10^{-8} Torr. Device characteristics were measured under illumination by a simulated 100 mW cm^{-2} AM1.5G light source using a 300 W Xe arc lamp with an AM 1.5 global filter using an aperture to define a device area of 0.13 cm^2. Solar-simulator irradiance was calibrated using a standard silicon photovoltaic cell with a protective KG1 filter calibrated by the National Renewable Energy Laboratory. In order to collect the data in Figure 5 devices were annealed at a given temperature for 2 min in a nitrogen environment, tested, annealed at a subsequently higher temperature for 2 min in a nitrogen environment, retested, and so forth, until all data had been collected at each temperature value.

Single Carrier Diode Fabrication and Testing: Electron only diodes were fabricated using a Si/SiO_2/PEDOT:PSS/Al (30 nm)/BHJ blend/Ca (10 nm)/Al (60 nm) architecture.[42] For in-situ thermal annealing measurements, diodes were measured using a Lake Shore Desert Cryogenics Division probe station evacuated to approximately 10^{-7} Torr. Samples were secured to the heating block using double sided carbon tape. The trend in electron mobility vs. temperature exhibited in Figure 4 was observed in multiple samples measured on multiple days.

Supporting Information

Supporting Information is available from the Wiley Online Library or from the author.

Acknowledgements

The authors thank NSF-DMR-SOLAR (#1035480) for support and funding. A.S. would like to acknowledge support from a National Science Foundation Graduate Research Fellowship. Portions of this research were conducted at the Stanford Synchrotron Radiation Lightsource user facility, operated by Stanford University on behalf of the U.S. Department of Energy, Office of Basic Energy Sciences and at the Advanced Photon Source (APS). APS is supported by the Director, Office of Science, Office of Basic Energy Sciences, of the U.S. Department of Energy under Contract No. DE-AC02–05CH11231. The authors would like to thank APS beamline scientist Joseph Strzalka for crucial assistance with GISAXS data collection and helpful discussions as well as Alexander Mikhailovsky for photoluminescence data acquisition. T.Q.N. thanks the Camille Dreyfus Teacher Scholar Award.

Received: December 6, 2013
Revised: January 16, 2014
Published online: February 28, 2014

[1] F. C. Krebs, S. A. Gevorgyan, J. Alstrup, *J. Mater. Chem.* **2009**, *19*, 5442.
[2] B. Azzopardi, C. J. M. Emmott, A. Urbina, F. C. Krebs, J. Mutale, J. Nelson, *Energy Environ. Sci.* **2011**, *4*, 3741.
[3] C. M. Proctor, M. Kuik, T.-Q. Nguyen, *Prog. Polym. Sci.* **2013**, *38*, 1941.
[4] B. A. Collins, Z. Li, J. R. Tumbleston, E. Gann, C. R. McNeill, H. Ade, *Adv. Energy Mater.* **2013**, *3*, 65.
[5] A. A. Bakulin, J. C. Hummelen, M. S. Pshenichnikov, P. H. M. van Loosdrecht, *Adv. Funct. Mater.* **2010**, *20*, 1653.
[6] N. D. Treat, M. A. Brady, G. Smith, M. F. Toney, E. J. Kramer, C. J. Hawker, M. L. Chabinyc, *Adv. Energy Mater.* **2011**, *1*, 82.
[7] D. Chen, F. Liu, C. Wang, A. Nakahara, T. P. Russell, *Nano Lett.* **2011**, *11*, 2071.
[8] D. R. Kozub, K. Vakhshouri, L. M. Orme, C. Wang, A. Hexemer, E. D. Gomez, *Macromolecules* **2011**, *44*, 5722.
[9] N. D. Treat, A. Varotto, C. J. Takacs, N. Batara, M. Al-Hashimi, M. J. Heeney, A. J. Heeger, F. Wudl, C. J. Hawker, M. L. Chabinyc, *J. Am. Chem. Soc.* **2012***134,* 15869.
[10] W. Ma, L. Ye, S. Zhang, J. Hou, H. Ade, *J. Mater. Chem. C* **2013**, *1*, 5023.
[11] W. Ma, J. R. Tumbleston, M. Wang, E. Gann, F. Huang, H. Ade, *Adv. Energy Mater.* **2013**, *3*, 864.
[12] J. R. Tumbleston, A. C. Stuart, E. Gann, W. You, H. Ade, *Adv. Funct. Mater.* **2013**, *23*, 3463.
[13] B. C. Thompson, J. M. J. Fréchet, *Angew. Chem. Int. Ed.* **2008**, *47*, 58.
[14] T. S. van der Poll, J. A. Love, T.-Q. Nguyen, G. C. Bazan, *Adv. Mater.* **2012**, *24*, 3646.
[15] J. Zhou, Y. Zuo, X. Wan, G. Long, Q. Zhang, W. Ni, Y. Liu, Z. Li, G. He, C. Li, B. Kan, M. Li, Y. Chen, *J. Am. Chem. Soc.* **2013**, *135*, 8484.
[16] B. Walker, A. B. Tamayo, X. Dang, P. Zalar, J. H. Seo, A. Garcia, M. Tantiwiwat, T. Nguyen, *Adv. Funct. Mater.* **2009**, *19*, 3063.
[17] X.-D. Dang, A. B. Tamayo, J. Seo, C. V. Hoven, B. Walker, T.-Q. Nguyen, *Adv. Funct. Mater.* **2010**, *20*, 3314.
[18] P. Müller-Buschbaum, *Adv. Mater.* **2014**, DOI: 10.1002/adma.201304187.
[19] M. L. Chabinyc, *Polym. Rev.* **2008**, *48*, 463.

[20] G. Renaud, R. Lazzari, F. Leroy, *Surf. Sci. Rep.* **2009**, *64*, 255.
[21] E. Verploegen, R. Mondal, C. J. Bettinger, S. Sok, M. F. Toney, Z. Bao, *Adv. Funct. Mater.* **2010**, *20*, 3519.
[22] A. Siciliano, A. Seves, T. D. Marco, S. Cimmino, E. Martuscelli, C. Silvestre, *Macromolecules* **1995**, *28*, 8065.
[23] L. Zhang, S. H. Goh, S. Y. Lee, *Polymer* **1998**, *39*, 4841.
[24] Methods of X-Ray and Neutron Scattering in Polymer Science (Ed: R. J. Roe), Oxford University Press, Inc., UK **2000**.
[25] Y. Zhou, K. Tvingstedt, F. Zhang, C. Du, W.-X. Ni, M. R. Andersson, O. Inganäs, *Adv. Funct. Mater.* **2009**, *19*, 3293.
[26] K. Tvingstedt, K. Vandewal, A. Gadisa, F. Zhang, J. Manca, O. Inganäs, *J. Am. Chem. Soc.* **2009**, *131*, 11819.
[27] K. Tvingstedt, K. Vandewal, F. Zhang, O. Inganäs, *J. Phys. Chem. C* **2010**, *114*, 21824.
[28] I. Riisness, M. J. Gordon, *Appl. Phys. Lett.* **2013**, *102*, 113302.
[29] V. D. Mihailetchi, J. K. J. van Duren, P. W. M. Blom, J. C. Hummelen, R. A. J. Janssen, J. M. Kroon, M. T. Rispens, W. J. H. Verhees, M. M. Wienk, *Adv. Funct. Mater.* **2003**, *13*, 43.
[30] N. I. Craciun, J. Wildeman, P. W. M. Blom, *Phys. Rev. Lett.* **2008**, *100*, 056601.
[31] C. M. Proctor, C. Kim, D. Neher, T.-Q. Nguyen, *Adv. Funct. Mater.* **2013**, *23*, 3584.
[32] A. Wagenpfahl, C. Deibel, V. Dyakonov, *IEEE J. Sel. Top. Quantum Electron.* **2010**, *16*, 1759.
[33] J. A. Bartelt, Z. M. Beiley, E. T. Hoke, W. R. Mateker, J. D. Douglas, B. A. Collins, J. R. Tumbleston, K. R. Graham, A. Amassian, H. Ade, J. M. J. Fréchet, M. F. Toney, M. D. McGehee, *Adv. Energy Mater.* **2012**, *3*, 364.
[34] K. Vakhshouri, D. R. Kozub, C. Wang, A. Salleo, E. D. Gomez, *Phys. Rev. Lett.* **2012**, *108*, 026601.
[35] L. Mandelkern, Crystallization of Polymers 2nd ed., Cambridge University Press, **2004**, Vol. *2*: Kinetics and Mechanisms.
[36] M. R. Hammond, R. J. Kline, A. A. Herzing, L. J. Richter, D. S. Germack, H.-W. Ro, C. L. Soles, D. A. Fischer, T. Xu, L. Yu, M. F. Toney, D. M. DeLongchamp, *ACS Nano* **2011**.
[37] J. Love, C. Proctor, J. Liu, C. Takacs, A. Sharenko, T. van der Poll, A. Heeger, G. Bazan, T.-Q. Nguyen, *Adv. Funct. Mater.* **2013**, *23*, 5019.
[38] V. S. Gevaerts, E. M. Herzig, M. Kirkus, K. H. Hendriks, M. M. Wienk, J. Perlich, P. Müller-Buschbaum, R. A. J. Janssen, *Chem. Mater.* **2014**, *26*, 916.
[39] L. A. Perez, K. W. Chou, J. A. Love, T. S. van der Poll, D.-M. Smilgies, T.-Q. Nguyen, E. J. Kramer, A. Amassian, G. C. Bazan, *Adv. Mater.* **2013**, *25*, 6380.
[40] G. C. Welch, L. A. Perez, C. V. Hoven, Y. Zhang, X.-D. Dang, A. Sharenko, M. F. Toney, E. J. Kramer, T.-Q. Nguyen, G. C. Bazan, *J. Mater. Chem.* **2011**, *21*, 12700.
[41] J. Ilavsky, *J. Appl. Crystallogr.* **2012**, *45*, 324.
[42] R. Steyrleuthner, S. Bange, D. Neher, *J. Appl. Phys.* **2009**, *105*, 064509.